

Frustration enhanced by Kitaev-exchange in a $\tilde{j}_{\text{eff}} = \frac{1}{2}$ triangular antiferromagnet

C. Wellm,^{1,2} W. Roscher,¹ J. Zeisner,^{1,2} A. Alfonsov,¹ R. Zhong,³ R. J. Cava,³
A. Savoyant,⁴ R. Hayn,^{1,4} J. van den Brink,^{1,5} B. Büchner,^{1,5} O. Janson,¹ and V. Kataev¹

¹*Leibniz Institute for Solid State and Materials Research IFW Dresden, 01171 Dresden, Germany*

²*Institute for Solid State and Materials Physics, TU Dresden, 01069 Dresden, Germany*

³*Department Of Chemistry, Princeton University, Princeton, NJ 08544, USA*

⁴*Aix-Marseille Univ., CNRS, IM2NP-UMR 7334, 13397 Marseille Cedex 20, France*

⁵*Würzburg-Dresden Cluster of Excellence ct.qmat, TU Dresden, D-01062 Dresden, Germany*

(Dated: March 27, 2022)

Triangular Heisenberg antiferromagnets are prototypes of geometric frustration, even if for nearest-neighbor interactions quantum fluctuations are not usually strong enough to destroy magnetic ordering: stronger frustration is required to stabilize a spin-liquid phase. On the basis of static magnetization and ESR measurements, we demonstrate the emergence of $\tilde{j}_{\text{eff}} = \frac{1}{2}$ moments in the triangular-lattice magnet $\text{Na}_2\text{BaCo}(\text{PO}_4)_2$. These moments are subject to an extra source of frustration that causes magnetic correlations to set in far above both the magnetic ordering and Weiss temperatures. Corroborating the $\tilde{j}_{\text{eff}} = \frac{1}{2}$ ground state, theory identifies ferromagnetic Kitaev exchange anisotropy as additional frustrating agent, altogether putting forward $\text{Na}_2\text{BaCo}(\text{PO}_4)_2$ as a new, promising Kitaev spin-liquid material.

Introduction. Quantum spin liquids are of topical interest as a promising host for fractionalized quasiparticles [1–5]. The quest for a spin-liquid ground state goes back to Anderson’s conjecture on resonating valence bonds (RVB) in the geometrically frustrated two-dimensional (2D) triangular lattice [6]. It is now firmly established, however, that the pure spin 1/2 triangular-lattice Heisenberg model has an ordered ground state [7]. This seemingly frustrating result is a blessing in disguise, though, as subsequent studies of modified triangular-lattice models found that long-range ordering can be suppressed by three disparate alterations: additional second-neighbor exchange [8–13], spatial anisotropy [14, 15], and exchange anisotropy [16, 17]. These findings opened new perspectives for realizing a spin-liquid state in the triangular lattice geometry, and boosted the search for candidate materials.

A recent breakthrough in triangular-lattice magnets pertains to the discovery of two material classes [18]. The first group of candidate materials are 4f magnets with Yb^{3+} : YbMgGaO_4 [19, 20] and NaYbX_2 (with $X=\text{O}, \text{S}, \text{Se}$) [21]. The key element of their physics is the crystal-field splitting of Yb^{3+} , giving rise to the ground-state doublet and hence the effective spin 1/2 behavior at low temperatures, and, in the former material, the significant effects of chemical disorder between the magnetic layers [22]. A similar scenario, with the lowest-lying doublet dominating the low-temperature physics, is realized in the other promising group of materials – Co^{2+} cobaltates. Here, the ground state doublet is stabilized by the spin orbit coupling as long as the low-symmetry crystal field distortions remain small (Fig. 1, a). Despite the overall tendency towards ferromagnetic exchange, several cobaltates with antiferromagnetic interactions are known. The most studied material of this handful, $\text{Ba}_3\text{CoSb}_2\text{O}_9$, shows intriguing high-field behav-

ior [23–25], but evades the spin-liquid regime by developing a long-range order at 3.7 K [23]. Interestingly, in the related layered honeycomb magnet $\text{BaCo}_2(\text{AsO}_4)_2$ the magnetic order can be suppressed by a low magnetic field yielding a nonmagnetic material [26].

The recently synthesized cobaltate $\text{Na}_2\text{BaCo}(\text{PO}_4)_2$ (Fig. 1, b) is a promising candidate for realization of a spin-liquid state on a triangular lattice. The first experimental study reported a sizable antiferromagnetic exchange and no long-range ordering down to 50 mK [27]. Very recently, ultralow-temperature specific heat measurements revealed a magnetic ordering transition at $T_N = 148$ mK [28], i.e., ~ 20 times smaller than the Weiss temperature $\theta = -2.5$ K obtained from the static magnetic susceptibility $\chi(T)$ [28]. Another interesting observation is the linear dependence of the residual thermal conductivity [28], compatible with the spinon Fermi surface scenario advocated for critical spin liquids. However, the microscopic model for $\text{Na}_2\text{BaCo}(\text{PO}_4)_2$ remains hitherto unexplored.

In this Letter, we fill this gap and demonstrate that exchange anisotropy stabilizes the spin-liquid behavior in $\text{Na}_2\text{BaCo}(\text{PO}_4)_2$ over a temperature range spanning two orders of magnitude. Our Co^{2+} electron spin resonance (ESR) measurements firmly establish the effective spin 1/2 state of the Co^{2+} ions by determining the g factor tensor and evaluating the excitation energy of the first excited state with effective spin 3/2. Further, the ESR data indicate the onset of magnetic correlations at the surprisingly high temperature of ~ 20 K, which is two orders of magnitude larger than T_N . Hence, magnetic correlations in this material build up far above the phenomenological energy scale set by the moderate Weiss temperature and the low saturation field of the magnetization. To reconcile these seemingly conflicting observations, we perform a microscopic analysis based

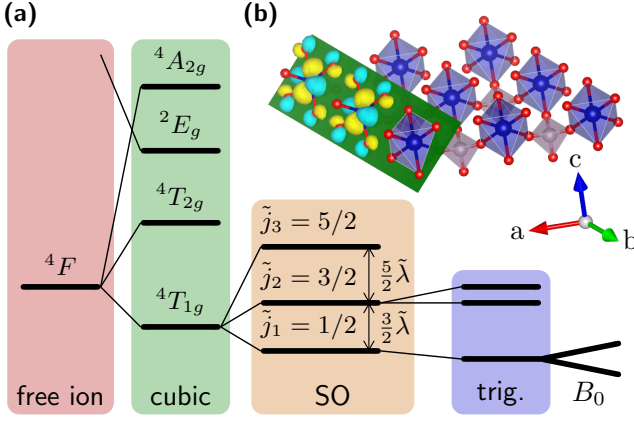


FIG. 1. (a) Energy diagram showing the splitting of the $4F$ state of Co^{2+} in a cubic crystal field, the spin-orbit (SO) coupling, trigonal distortion and the Zeeman splitting due to the magnetic field B_0 in the $4T_{1g}$ multiplet. (b) Fragment of a triangular layer in the $\text{Na}_2\text{BaCo}(\text{PO}_4)_2$ crystal structure, with CoO_6 octahedra bridged by PO_4 tetrahedra. For a pair of neighboring Co atoms, the leading contribution to hopping stems from the depicted Wannier functions. Note that the respective Co d orbitals lie in the same plane.

on density-functional-theory (DFT) band-structure and multiplet calculations. We confirm the effective spin $1/2$ (hereafter $\tilde{j}_{\text{eff}} = \frac{1}{2}$) behavior, estimate theoretically the g factors, and justify the restriction of the magnetic system to the strong dominance of the nearest-neighbor exchange J_1 , which however turns out to be substantially larger than previous experimental estimates. By applying perturbation-theory expressions from Ref. [8, 29] to the multi-orbital Hubbard model parameterized by DFT calculations, we conclude that $\text{Na}_2\text{BaCo}(\text{PO}_4)_2$ features a substantial ferromagnetic Kitaev exchange K_1 . The competition of antiferromagnetic J_1 and ferromagnetic K_1 lowers the saturation field and the Weiss temperature, but promotes the build-up of magnetic correlations to higher temperatures.

Experimental results. Magnetization and ESR experiments were conducted on both powder and single crystal samples of $\text{Na}_2\text{BaCo}(\text{PO}_4)_2$ synthesized and thoroughly characterized in Ref. [27]. Representative magnetization $M(H)$ and the inverse susceptibility $\chi^{-1}(T) = H/M(T)$ curves are shown in Fig. 2.

The $M(H)$ dependence can be well fitted to the equation $M = g\tilde{j}_{\text{eff}}B_{1/2}((H_0 + H_{\text{ex}}), T) + \chi_0 H_0$. Here, $B_{1/2}$ is the Brillouin function for spin $1/2$, g is the g factor, H_0 is the external magnetic field, χ_0 accounts for the van Vleck and diamagnetic susceptibility, and $H_{\text{ex}} = a_{\text{ex}}M$ is the exchange field with the parameter a_{ex} characterizing the strength of the isotropic exchange interaction $J = a_{\text{ex}}g^2\mu_B/N_{\text{NN}}$ with N_{NN} being the number of next neighbors. A representative fit for the powder sample is shown in the main panel of Fig. 2(a). It yields antiferromagnetic (AFM) $J = 1.37$ K and a g factor $g_{\text{P}}^M = 4.38$. For the

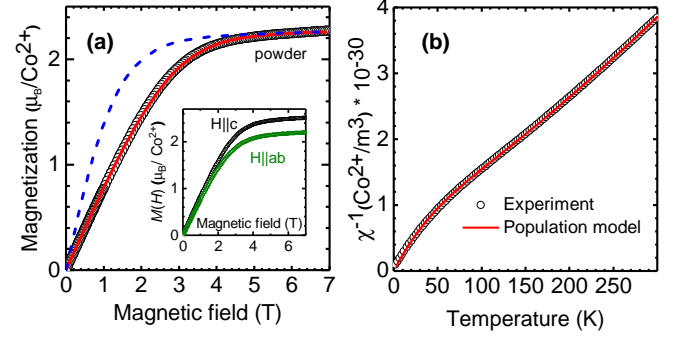


FIG. 2. (a) Main panel: Powder $M(H)$ dependence at $T = 2$ K (data points). A delayed increase of the $M(H)$ curve compared to the Brillouin function of noninteracting spins $S = 1/2$ (dashed curve) indicates a sizable AFM interaction. Accounting for it, as explained in the text, yields a good agreement with the experiment (red solid curve); Inset: Single crystalline $M(H)$ dependence for $\mathbf{H} \parallel c$ axis and $\mathbf{H} \parallel ab$ plane. (b) Powder $\chi^{-1}(T)$ dependence at $\mu_0 H = 20$ mT (data points). Solid line depicts the calculated curve according to the population model (see the text).

single crystal, the g factors were found to be $g_c^M = 4.81$ and $g_{\text{ab}}^M = 4.22$. The slight g factor anisotropy is likely related to a small trigonal distortion of the CoO_6 octahedra [3].

The inverse susceptibility $\chi^{-1}(T)$ per Co^{2+} ion at $\mu_0 H = 20$ mT is shown in Fig. 2(b) together with the result of a population model. The latter is derived from the diagonalization of a single-ion Hamiltonian including the spin-orbit coupling and the Zeeman interactions, $\mathcal{H} = \lambda \mathbf{S} \cdot \mathbf{L} - \mu_B B (g_S S_z + g_L L_z)$ with $g_S = 2$, $g_L = -3/2$ and thermal average $\langle M \rangle = \mathcal{Z}^{-1} \sum_i \langle E_i | e^{-E_i/k_B T} \mu_z | E_i \rangle$, \mathcal{Z} being the partition sum. $\chi^{-1}(T)$ does not obey a simple Curie-Weiss (CW) law $\propto T$, but rather possesses a remarkable inflection point around $T \sim 150$ K which is reasonable to attribute to the thermally assisted population of the excited $\tilde{j}_2 = \frac{3}{2}$ multiplet (Fig. 1). The modeling reproduces the experimental data with the energy splitting $\Delta E_{\tilde{j}_1, \tilde{j}_2} = E_{\tilde{j}_2} - E_{\tilde{j}_1} = 419$ K.

The main results of the ESR measurements for both the powder- and single-crystalline samples at the X-band frequency of $\nu = 9.6$ GHz conducted with a commercial ESR spectrometer from Bruker are summarized in Figs. 3(a) and (b). A rather broad Lorentzian-shaped signal was observed [Fig. 3(a)]. The Lorentzian fitting yielded the width ΔH and the resonance field H_{res} from which the effective g factor can be calculated according to resonance condition $h\nu = g\mu_B H_{\text{res}}$.

The angular dependent measurements revealed an anisotropy of the g factor which follows the conventional angular dependence $g(\alpha) = \sqrt{g_{\text{ab}}^2 \cos^2(\alpha) + g_c^2 \sin^2(\alpha)}$ with α being the angle which the applied field makes with the c axis [Fig. 3(a), inset]. The fit yielded the values $g_c \approx 4.83$ and $g_{\text{ab}} \approx 4.42$ for the out-of-plane and

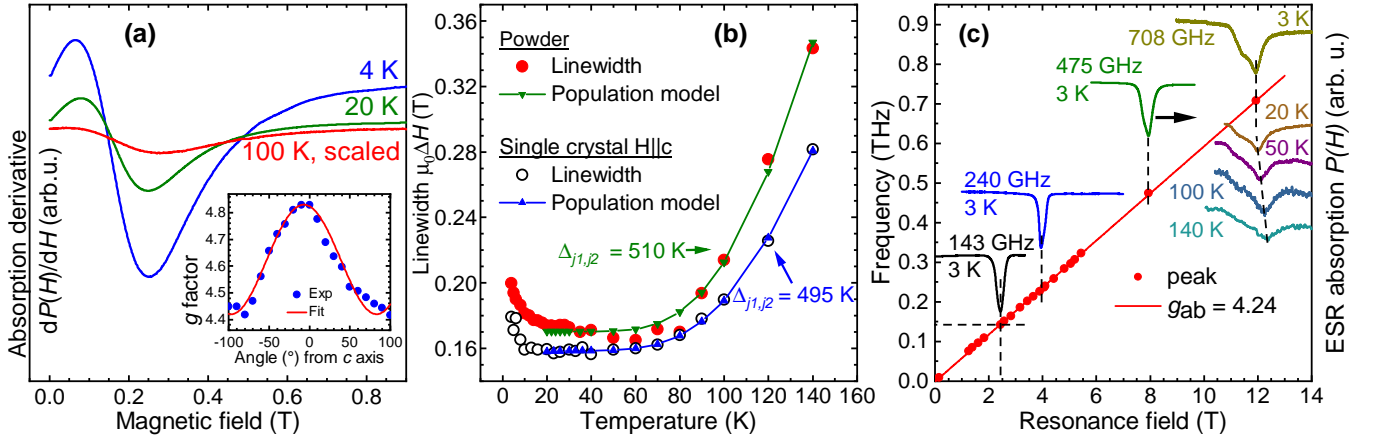


FIG. 3. (a) Single crystalline ESR signals (field derivative of the microwave absorption) at $\nu = 9.6$ GHz for $\mathbf{H} \parallel c$ axis at selected temperatures. Inset: Angular dependence of the g factor at $\nu = 9.6$ GHz and at $T = 4$ K (data points). Solid line is a fit to the dependence $g(\alpha) = [g_{ab}^2 \cos^2(\alpha) + g_c^2 \sin^2(\alpha)]^{1/2}$; (b) T -dependence of the ESR linewidth of the single- and polycrystalline samples at $\nu = 9.6$ GHz (data points). Solid lines are the calculated dependences according to the population model (see the text); (c) Left scale: ν vs. field position of the peak of the powder HF-ESR spectrum at $T = 3$ K (dots). Solid line is the fit to the dependence $h\nu = g_{ab}\mu_B H$; Right scale: Powder HF-ESR spectra at selected frequencies ν at $T = 3$ K and at selected temperatures at $\nu = 708$ GHz.

in-plane orientation of the field, respectively, consistent with the static magnetization data.

More accurate estimates of the g_{ab} value were provided by multi-frequency high-field ESR (HF-ESR) measurements on the powder sample which were carried out with a homemade setup [32]. Selected HF-ESR spectra at $T = 3$ K and different excitation frequencies are shown in Fig. 3(c). The signal is a single Lorentzian-shaped line at lower frequencies and develops a shoulder at $\nu \geq 150$ GHz. Such a structure typical of the ESR response of a powder sample with an anisotropic g factor [33] can be most clearly resolved at the highest frequency of 708 GHz. In the case of the uniaxial g anisotropy the resonance field of the peak is determined by the g factor component perpendicular to the symmetry axis, i.e., by g_{ab} in our case [33]. The field position of the peak plotted *versus* ν exhibits a linear dependence according to the relation $h\nu = g_{ab}\mu_B H$ and gives $g_{ab}^{\text{HF}} = 4.24$ [Fig. 3(c)]. Note that this linear dependence features a negligible intercept with the frequency axis evidencing the absence of any gap in the uniform spin excitation spectrum larger than 9.6 GHz (0.04 meV). Thus, taken together the X-band and HF-ESR results yield the \mathbf{g} tensor $[g_c, g_{ab}] = [4.83, 4.24]$ consistent with the estimate $[g_c^M, g_{ab}^M] = [4.81, 4.22]$ from the magnetization data. Interestingly, with increasing the temperature close to 100 K the peak of the HF-ESR spectrum at $\nu = 708$ GHz shifts by an amount of $\mu_0 \delta H_0 \approx 0.35$ T towards higher fields, suggesting a reduction of the g factor [Fig. 3(c)]. At $T = 100$ K, a linear ν *versus* H g factor fit of this peak yields $g_c(100\text{ K}) = 4.11$. Such a reduction indicates the involvement of the thermally-populated excited $\tilde{j}_2 = \frac{3}{2}$ multiplet which is characterized by a smaller

g factor [3].

Both X-band and HF-ESR spectra broaden significantly with increasing the temperature [Figs. 3(a) and (c)]. Analysis of the origin of this broadening provides important insights into the spin dynamics and temperature effects in $\text{Na}_2\text{BaCo}(\text{PO}_4)_2$. On the quantitative level, the $\Delta H(T)$ dependence can be more accurately evaluated from the X-band data because strong fields applied in an HF-ESR experiment may cause additional inhomogeneous broadening, and instrumental distortions of the lineshape are possible in the HF-ESR apparatus.

In Fig. 3(b), the temperature dependence of the linewidth, as obtained from the Lorentzian fits, is shown for the powder- and single-crystalline samples. While lowering the temperature the width decreases down to approximately 50 K, then remains constant until approximately 20 K, where it starts to rise again. The high-temperature behavior is likely due to the above discussed population effect of the excited $\tilde{j}_2 = \frac{3}{2}$ multiplet [Fig. 1(a)]. This leads to a broadening of the linewidth, while at lower temperatures, only the $\tilde{j}_1 = \frac{1}{2}$ multiplet is populated. This behavior can be reproduced by a population model with Boltzmann weights for the energy levels of the Co^{2+} ions in an octahedral oxygen environment, as described in [34]. From this model, one obtains the energy splitting $\Delta E_{\tilde{j}_1, \tilde{j}_2}^{\text{pow}} = 510$ K for the powder sample, which is somewhat larger than the estimate from the modeling of the static susceptibility. For the single crystal, one has, similarly, $\Delta E_{\tilde{j}_1, \tilde{j}_2}^{\text{cr}} = 495$ K. For the in-plane direction of the field, the linewidth could not be modeled well due to the uncertainty of the Lorentzian fits.

The upturn of $\Delta H(T)$ below 20 K is remarkable. It cannot be described by the single-ion population model

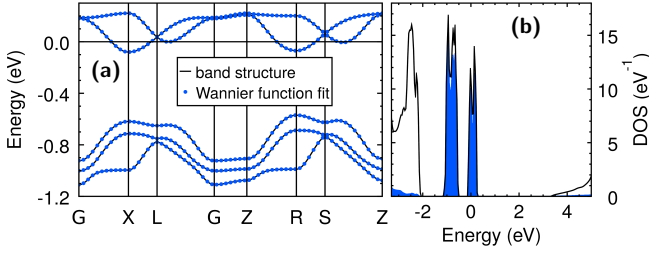


FIG. 4. (a) GGA band structure (lines) and the eigenvalues of the Fourier-transformed Wannier Hamiltonian (circles). Note that all bands are doubly degenerate due to the time-reversal symmetry. (b) GGA density of states (DOS). Co 3d contributions are shown shaded. The Fermi level is at zero energy.

suggesting that magnetic correlations between the Co spins begin to develop gradually. Usually this signifies proximity to a magnetic phase transition where the spin dynamics experiences a critical slowing down [35]. However, such a phase transition in $\text{Na}_2\text{BaCo}(\text{PO}_4)_2$ takes place at two orders of magnitude lower temperature of $T_N = 148 \text{ mK}$ [28] which evidences an extended low-temperature regime of the spin-liquid like, slow spin fluctuations in the electron spin system.

Theory and discussion. To understand why magnetic correlations set on at such a high temperature, we performed a microscopic numerical analysis based on DFT band-structure as well as multiplet calculations. For the former, we do full-relativistic nonmagnetic DFT calculations within the generalized gradient approximation (GGA) [36], as implemented in the full-potential local-orbital code FPLO [37]. As an input, we use the experimental crystal structure described within the space group $P\bar{3}m1$ [27]. The unit cell contains one Co atom with the local trigonal symmetry (point group $3m$). The GGA band structure features a ten-band manifold crossing the Fermi level, as expected for a unit cell containing one Co atom featuring five d orbitals and two spins flavors. In the absence of spin polarization, each band is doubly degenerate in accord with the Kramers theorem. As a result, the band structure features only five distinct band dispersions (Fig. 4, a). The strong octahedral crystal field splits these bands into two manifolds that are well-separated from the rest of the valence band and are formed almost exclusively by Co d states (Fig. 4, b) [38]. For further analysis, we single out these states by resorting to Co-centered Wannier functions (WF). Following the procedure described in Ref. [39], we obtain excellent agreement between the Fourier-transformed WF and the respective GGA bands (Fig. 4, a).

In the WF basis, the Hamiltonian is a sum of local and nonlocal terms. The former describes the one-particle spectrum of an isolated trigonally-distorted CoO_6 octahedron, and key parameters of the local Hamiltonian can be extracted directly from WF [40]. By inspecting different contributions, we find a well-defined hierarchy of

energy scales: the strong cubic crystal field (CF), followed by the spin-orbit (SO) interactions, the trigonal CF splitting, and finally, the Zeeman term. The separation of energy scales allows us to disentangle the underlying processes and arrive at an intuitive physical picture, which we show in Fig 1(a). First, the cubic CF splits the 4F multiplet of the free Co^{2+} ion into three multiplets where the lower one, $^4T_{1g}$, contains predominantly only one-electron t_{2g} holes. Next, the $^4T_{1g}$ multiplet is further split by the SO interaction. An isolated $^4T_{1g}$ multiplet can be solved analytically [3] resulting in effective \tilde{j} values, from lowest to highest energy $\tilde{j}_1 = \frac{1}{2}$, $\tilde{j}_2 = \frac{3}{2}$ and $\tilde{j}_3 = \frac{5}{2}$ [41]; the respective g -factors amount to $g_1 = \frac{13}{3}$, $g_2 = \frac{16}{15}$ and $g_3 = \frac{3}{5}$, and the two splittings amount to $\frac{3}{2}\tilde{\lambda}$ and $\frac{5}{2}\tilde{\lambda}$, where $\tilde{\lambda} = 33 \text{ meV}$ is the effective SO interaction parameter [42]. The trigonal CF further splits the second and third multiplets, giving rise to the experimentally observed g factor anisotropy. Finally, the Zeeman interaction lifts the remaining degeneracy.

The GGA calculations (Fig. 4) imply a one-electron picture in an effective mean-field potential and cannot display the multiplet structure directly. To account for the ensuing electronic correlations, we perform multiplet calculations using the parameters extracted from the WF, and obtain a complete numerical solution of the local many-body problem. Skipping methodological aspects of this procedure that will be published elsewhere, we go straight to the most important result: the splitting between the $\tilde{j}_1 = \frac{1}{2}$ ground state and the lowest-lying $\tilde{j}_2 = \frac{3}{2}$ component amounts to $\Delta E_{\tilde{j}_1, \tilde{j}_2} = 472 \text{ K}$, in a fair agreement with our experimental estimates [43]. The splitting exceeds by far the magnetic energy scale. Therefore, the magnetism of $\text{Na}_2\text{BaCo}(\text{PO}_4)_2$ can be safely described in an effective $\tilde{j}_{\text{eff}} = \frac{1}{2}$ model. Another important observable is the \mathbf{g} tensor anisotropy, i.e. the difference between g_c and g_{ab} . Our calculations lead to an anisotropy of $g_c = 4.33$ and $g_{ab} = 4.55$ being slightly smaller than the experimental one and of opposite sign. The reason for this discrepancy is the extreme sensitivity of the g factor anisotropy to the small (10 meV) trigonal crystal field parameter: a small readjustment of the CF parameter reproduces the experimental values ($g_c^{\text{adj}} = 4.80$ and $g_{ab}^{\text{adj}} = 4.31$). And since the trigonal CF is in turn governed by the oxygen positions in the crystal structure, additional structural refinements, especially at lower temperatures, are needed for a conclusive analysis.

Having solved the local problem, we turn to hopping processes that underlie the magnetic exchange. By analysing the respective WF, we find that $\text{Na}_2\text{BaCo}(\text{PO}_4)_2$ is an excellent model system: further longer-range in-plane as well as interplane hoppings are orders of magnitude weaker than the leading nearest-neighbor terms. As we are dealing with a multi-orbital problem, a direct determination of the magnetic exchange integrals from the hopping terms is very chal-

lenging. Therefore, we start with a qualitative analysis. By inspecting the hoppings between different orbitals, we find that for every pair of neighboring Co atoms, the leading contribution pertains to a single matrix element: virtual electron transfer between two t_{2g} orbitals lying in the same plane [e.g., the plane in Fig. 1(b)] being denoted as t' in Refs. [8, 29]. We note that this hopping is underlain by the perfect mutual alignment of neighboring CoO_6 octahedra and may be strongly suppressed if the octahedra are tilted.

Next, we estimate the exchange integral J_1 quantitatively. To this end, we perform full-relativistic magnetic DFT+ U calculations [43]. We find that large orbital moments, a prerequisite for the correct description of $\tilde{j}_{\text{eff}} = \frac{1}{2}$ physics, are stable only if the quantization axis coincides with the threefold rotation crystal axis. We construct three supercells and perform total-energy calculations for different collinear magnetic arrangements. By mapping the total energies onto a classical Heisenberg model with effective spins $\tilde{j}_{\text{eff}} = \frac{1}{2}$, we estimate the nearest-neighbor exchange to be 11.6 ± 2.0 K, where the error bars pertain to the uncertainty in choosing the U value ($U = 5 \mp 1$ eV).

Why is the DFT+ U estimate for J_1 so large? To find the root cause, we first recollect that the magnetic exchange in $\text{Na}_2\text{BaCo}(\text{PO}_4)_2$ is anisotropic. As the orientation of magnetic moments in DFT+ U is fixed, such calculations provide only one component of the magnetic exchange, J_1^{zz} . To estimate the anisotropic terms we go a step back and apply the recently developed perturbative expressions, [8, 29] parameterized by our WF. Using just the dominant hopping term $t' = 82$ meV we arrive at $J_1^{zz} = J_1 + K_1/3 = 2.3$ K, which is smaller than the DFT+ U estimate. Surprisingly, we find, besides the leading antiferromagnetic term $J_1 = (16/81)(t')^2/U = 3.1$ K, also a sizable ferromagnetic Kitaev term $K_1 = (-4/27)(t')^2/U = -2.3$ K. Other anisotropic terms are smaller, and hence nearest neighbor exchange and Kitaev terms dominate the magnetic interactions. These results agree with our mean-field estimate of J from the magnetization $M(H)$ dependence [Fig. 2(a)].

We are now in position to combine our results into a coherent physical picture. $\text{Na}_2\text{BaCo}(\text{PO}_4)_2$ is a nearest-neighbor $\tilde{j}_{\text{eff}} = \frac{1}{2}$ triangular magnet with a strongly anisotropic exchange: Its magnetism is driven by the competition of the dominant antiferromagnetic contribution with a sizable ferromagnetic Kitaev term. The latter lowers the saturation field, which otherwise would be of the order of J_1 . But the energy scale of magnetic correlations is set by the absolute values of magnetic exchanges, and hence it is enhanced by K_1 . Therefore, the onset of the spin-spin correlations already at $T \sim 20$ K $\gg T_N$, manifested in the observed broadening of the ESR linewidth, is a combined effect of J_1 and K_1 .

Conclusions. Our static magnetization and ESR results on the spin liquid candidate material

$\text{Na}_2\text{BaCo}(\text{PO}_4)_2$ enable to classify it as an anisotropic triangular magnet in the effective spin $\tilde{j}_{\text{eff}} = \frac{1}{2}$ ground state well isolated from the higher energy effective spin- $\frac{3}{2}$ state. Furthermore, the ESR data provide strong indications of the magnetic correlations setting in far above the magnetic ordering temperature T_N and the Weiss temperature θ . We established the anisotropic $\tilde{j}_{\text{eff}} = \frac{1}{2}$ ground state on the theory level as well and reveal, besides the antiferromagnetic isotropic nearest-neighbor exchange interaction J_1 , a significant ferromagnetic Kitaev interaction term K , which is beneficial for the realization of a spin liquid in this compound. The competition between J_1 and K reduces the temperature scale θ but does not affect magnetic correlations whose energy scale of ~ 20 K $\gg T_N$ is probed by ESR. Altogether our findings put forward $\text{Na}_2\text{BaCo}(\text{PO}_4)_2$ as a new, promising Kitaev-exchange-assisted spin-liquid material and call for further extensive exploration of the exciting physics of this class of compounds.

Acknowledgments OJ thanks Alexander Tsirlin and RH thanks Roman Kuzian for fruitful discussions and helpful comments. We thank Manuel Richter for useful hints on DFT+ U calculations and Ulrike Nitzsche for technical assistance. WR and OJ were supported by the Leibniz Association through the Leibniz Competition. This work was supported in part by the Deutsche Forschungsgemeinschaft (DFG), grant number KA 1694/12-1. The materials synthesis was supported by the Gordon and Betty Moore Foundation, EPiQS Program, grant number GBMF-4412.

-
- [1] L. Balents, *Nature (London)* **464**, 199 (2010).
 - [2] L. Savary and L. Balents, *Rep. Progr. Phys.* **80**, 016502 (2016).
 - [3] Y. Zhou, K. Kanoda, and T.-K. Ng, *Rev. Mod. Phys.* **89**, 025003 (2017).
 - [4] J. Knolle and R. Moessner, *Ann. Rev. Condens. Matter Phys.* **10**, 451 (2019).
 - [5] C. Broholm, R. J. Cava, S. A. Kivelson, D. G. Nocera, M. R. Norman, and T. Senthil, *Science* **367**, 263 (2020).
 - [6] P. W. Anderson, *Mater. Res. Bull.* **8**, 153 (1973).
 - [7] B. Bernu, C. Lhuillier, and L. Pierre, *Phys. Rev. Lett.* **69**, 2590 (1992); B. Bernu, P. Lecheminant, C. Lhuillier, and L. Pierre, *Phys. Scripta* **T49**, 192 (1993); *Phys. Rev. B* **50**, 10048 (1994); S. R. White and A. L. Chernyshev, *Phys. Rev. Lett.* **99**, 127004 (2007).
 - [8] Y. Iqbal, W.-J. Hu, R. Thomale, D. Poilblanc, and F. Becca, *Phys. Rev. B* **93**, 144411 (2016).
 - [9] D.-V. Bauer and J. O. Fjærstad, *Phys. Rev. B* **96**, 165141 (2017).
 - [10] S. N. Saadatmand and I. P. McCulloch, *Phys. Rev. B* **96**, 075117 (2017).
 - [11] S.-S. Gong, W. Zhu, J.-X. Zhu, D. N. Sheng, and K. Yang, *Phys. Rev. B* **96**, 075116 (2017).
 - [12] F. Ferrari and F. Becca, *Phys. Rev. X* **9**, 031026 (2019).
 - [13] S. Hu, W. Zhu, S. Eggert, and Y.-C. He, *Phys. Rev. Lett.*

- 123**, 207203 (2019).
- [14] S. Yunoki and S. Sorella, *Phys. Rev. B* **74**, 014408 (2006).
 - [15] E. Ghorbani, L. F. Tocchio, and F. Becca, *Phys. Rev. B* **93**, 085111 (2016).
 - [16] Z. Zhu, P. A. Maksimov, S. R. White, and A. L. Chernyshev, *Phys. Rev. Lett.* **120**, 207203 (2018).
 - [17] P. A. Maksimov, Z. Zhu, S. R. White, and A. L. Chernyshev, *Phys. Rev. X* **9**, 021017 (2019).
 - [18] Y. Li, P. Gegenwart, and A. A. Tsirlin, *J. Phys.: Condens. Matter* **32**, 224004 (2020).
 - [19] Y. Li, H. Liao, Z. Zhang, S. Li, F. Jin, L. Ling, L. Zhang, Y. Zou, L. Pi, Z. Yang, J. Wang, Z. Wu, and Q. Zhang, *Sci. Rep.* **5**, 16419 (2015).
 - [20] Y. Li, G. Chen, W. Tong, L. Pi, J. Liu, Z. Yang, X. Wang, and Q. Zhang, *Phys. Rev. Lett.* **115**, 167203 (2015).
 - [21] W. Liu, Z. Zhang, J. Ji, Y. Liu, J. Li, X. Wang, H. Lei, G. Chen, and Q. Zhang, *Chinese Phys. Lett.* **35**, 117501 (2018).
 - [22] J. A. M. Paddison, M. Daum, Z. Dun, G. Ehlers, Y. Liu, M. B. Stone, H. Zhou, and M. Mouri, *Nature Phys.* **13**, 117 (2017).
 - [23] Y. Shirata, H. Tanaka, A. Matsuo, and K. Kindo, *Phys. Rev. Lett.* **108**, 057205 (2012).
 - [24] T. Susuki, N. Kurita, T. Tanaka, H. Nojiri, A. Matsuo, K. Kindo, and H. Tanaka, *Phys. Rev. Lett.* **110**, 267201 (2013).
 - [25] G. Koutroulakis, T. Zhou, Y. Kamiya, J. D. Thompson, H. D. Zhou, C. D. Batista, and S. E. Brown, *Phys. Rev. B* **91**, 024410 (2015).
 - [26] R. Zhong, T. Gao, N. P. Ong, and R. J. Cava, *Sci. Adv.* **6**, eaay6953 (2020).
 - [27] R. Zhong, S. Guo, G. Xu, Z. Xu, and R. J. Cava, *Proc. Nat. Acad. Sci.* **116**, 14505 (2019).
 - [28] N. Li, Q. Huang, X. Y. Yue, W. J. Chu, Q. Chen, E. S. Choi, X. Zhao, H. D. Zhou, and X. F. Sun, *Nat. Commun.* **11**, 4216 (2020).
 - [29] H. Liu and G. Khaliullin, *Phys. Rev. B* **97**, 014407 (2018).
 - [8] H. Liu, J. Chaloupka, and G. Khaliullin, *Phys. Rev. Lett.* **125**, 047201 (2020).
 - [3] A. Abragam and B. Bleaney, *Electron paramagnetic resonance of transition ions*, Oxford classic texts in the physical sciences (Oxford University Press, 1970).
 - [32] J. Zeisner, S. A. Bräuninger, L. Opherden, R. Sarkar, D. I. Gorbunov, J. W. Krizan, T. Herrmannsdörfer, R. J. Cava, J. Wosnitza, B. Büchner, H.-H. Klauss, and V. Kataev, *Phys. Rev. B* **99**, 155104 (2019).
 - [33] C. P. Poole, *Electron Spin Resonance: A Comprehensive Treatise on Experimental Techniques*, Dover books on physics (Dover Publications, 1996).
 - [34] C. Slichter, *Principles of Magnetic Resonance*, Springer Series in Solid-State Sciences (Springer Berlin Heidelberg, 1996).
 - [35] H. Benner and J. P. Boucher, Spin dynamics in the paramagnetic regime: NMR and EPR in two-dimensional magnets, in *Magnetic Properties of Layered Transition Metal Compounds*, edited by L. J. de Jongh (Springer Netherlands, Dordrecht, 1990) pp. 323–378.
 - [36] J. P. Perdew, K. Burke, and M. Ernzerhof, *Phys. Rev. Lett.* **77**, 3865 (1996).
 - [37] K. Koepnick and H. Eschrig, *Phys. Rev. B* **59**, 1743 (1999).
 - [38] Note that the band structure is based on the one-electron approach of DFT. There is no simple correspondence between the DFT picture and the ground-state multiplet in Fig. 1.
 - [39] H. Eschrig and K. Koepnick, *Phys. Rev. B* **80**, 104503 (2009).
 - [40] R. O. Kuzian, O. Janson, A. Savoyant, J. van den Brink, and R. Hayn, *Ab initio* ligand field approach to determine electronic multiplet properties (2021), [arXiv:2104.10090 \[cond-mat.str-el\]](https://arxiv.org/abs/2104.10090).
 - [41] Higher-lying multiplets shown in (Fig. 1, a) are irrelevant in the temperature and energy range of consideration.
 - [42] Note that three definitions of the SO coupling constant are used for cobaltates: ζ (for the one-electron picture), λ (for the many-body picture) and $\tilde{\lambda}$ (effective parameter for the orbital angular momentum equal to unity). For $d^7 \text{Co}^{2+}$, $\frac{\zeta}{3} \equiv -\lambda \equiv \frac{2}{3}\tilde{\lambda}$.
 - [43] See Supplemental Material for the matrix elements of the local Wannier Hamiltonian and of the nearest-neighbor hopping term, the dependence of the DFT+ U -derived magnetic exchange integrals on the U value, and details of the multiplet calculations by exact diagonalization.

Supplemental Material for
Frustration enhanced by Kitaev-exchange in a $\tilde{j}_{\text{eff}} = \frac{1}{2}$ triangular antiferromagnet

C. Wellm, W. Roscher, J. Zeisner, A. Alfonsov, R. Zhong, R. J. Cava,
A. Savoyant, R. Hayn, J. van den Brink, B. Büchner, O. Janson, and V. Kataev

WANNIER FUNCTIONS: LOCAL TERMS

We analyse the full-relativistic non spin-polarized GGA band structure of $\text{Na}_2\text{BaCo}(\text{PO}_4)_2$ (Fig. 4 in the manuscript) by constructing Wannier functions (WF) describing the Co $3d$ states. To this end, we resort to the trigonal basis:

$$\begin{aligned} |x\rangle &= \sqrt{\frac{2}{3}} |x^2 - y^2\rangle - \sqrt{\frac{1}{3}} |xz\rangle \\ |y\rangle &= -\sqrt{\frac{2}{3}} |xy\rangle - \sqrt{\frac{1}{3}} |yz\rangle \\ |z\rangle &= |z^2\rangle \\ |v\rangle &= \sqrt{\frac{1}{3}} |x^2 - y^2\rangle + \sqrt{\frac{2}{3}} |xz\rangle \\ |w\rangle &= -\sqrt{\frac{1}{3}} |xy\rangle + \sqrt{\frac{2}{3}} |yz\rangle, \end{aligned} \tag{1}$$

In this basis, the local terms of the resulting Hamiltonian are given by the following Hermitian matrix:

$$H_0 = \begin{pmatrix} \begin{matrix} +\frac{1}{2} & x & -\frac{1}{2} & +\frac{1}{2} & y & -\frac{1}{2} & +\frac{1}{2} & z & -\frac{1}{2} & +\frac{1}{2} & v & -\frac{1}{2} & +\frac{1}{2} & w & -\frac{1}{2} \end{matrix} \\ \begin{matrix} -793.8 & 0 & 32.9i & 0 & 0 & -33.8 & 10.7 & 33.5 & 47.4i & 33.5i \\ & -793.8 & 0 & -32.9i & 33.8 & 0 & -33.5 & 10.7 & 33.5i & -47.4i \\ & & -793.8 & 0 & 0 & 33.8i & -47.4i & 33.5i & 10.7 & -33.5 \\ & & & -793.8 & 33.8i & 0 & 33.5i & 47.4i & 33.5 & 10.7 \\ & & & & -804.4 & 0 & 0 & -47.5 & 0 & 47.5i \\ & & & & & -804.4 & 47.5 & 0 & 47.5i & 0 \\ & & & & & & 88.5 & 0 & 0 & 0 \\ & & & & & & & 88.5 & 0 & 0 \\ & & & & & & & & 88.5 & 0 \\ & & & & & & & & & 88.5 \end{matrix} \end{pmatrix}, \tag{2}$$

where we show only the upper triangular part. All values are in meV.

WANNIER FUNCTIONS: NEAREST-NEIGHBOR HOPPING

To describe the nearest-neighbor hopping t_1 , it is reasonable to resort to the standard d basis ($|xy\rangle$, $|yz\rangle$, $|3z^2 - r^2\rangle$, $|xz\rangle$, and $|x^2 - y^2\rangle$):

$$t_1 = \begin{pmatrix} -2.0 & -17.3 & 7.1 & 1.3 & 1.8 \\ & -2.0 & -2.0 & 1.3 & 7.0 \\ & & 33.8 & -8.0 & -31.2 \\ & & & -\mathbf{82.8} & -13.8 \\ & & & & -2.2 \end{pmatrix}. \tag{3}$$

Note that the matrix elements in Eq. (3) are given for the pair of Co atoms separated by the lattice translation vector a , i.e. along the crystallographic direction $[100]$.

EXCHANGE INTEGRALS FROM DFT+ U CALCULATIONS

We estimate the magnetic exchanges by solving a redundant system of linear equations parameterized by spin-polarized GGA+ U total energies. Full-relativistic SGGA+ U calculations are done using the fully-localized-limit double-counting correction with the onsite Coulomb repulsion of 3.5...6.5 eV and the onsite Hund's exchange of 1 eV. Figure 5 shows how the DFT+ U -evaluated magnetic exchanges depend on the Coulomb interaction U .

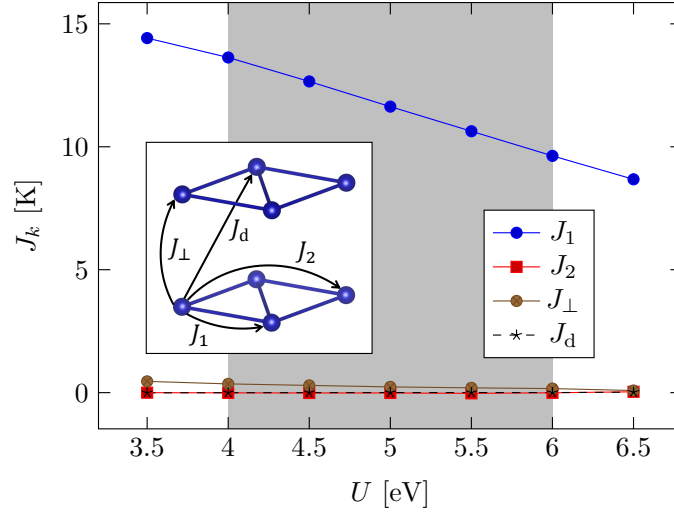


FIG. 5. The magnetic exchanges as a function of the onsite Coulomb repulsion U ; the shaded area demarcates the range of plausible values. The relevant exchange pathways are schematically depicted in the inset.

MULTIPLY CALCULATIONS BY EXACT DIAGONALIZATION

To calculate the multiplet spectrum of a single Co^{2+} center we treat a local Hamiltonian for the configuration $3d^7$, containing Coulomb, ligand field, and spin-orbit (SO) interactions, leading to a 120×120 matrix problem. The influence of the surrounding octahedra of O ligands with a slight trigonal distortion (point group D_{3d}) is taken into account by three ligand field (LF) parameters. The local single-ion Hamiltonian can be written as

$$H = H_{\text{Coul}} + H_{\text{LF}} + H_{\text{SO}} , \quad (4)$$

and it is diagonalized exactly using the computer code ELISA (electrons localized in single atoms) which was used before to calculate the X-ray absorption spectra (XAS) of Mn-TCNB (Mn-tetracyanobenzene) [1]. The Coulomb and spin-orbit interactions are treated as in rotationally invariant atoms. Its matrix elements are well known, and their parameters are fitted to the spectra for a free Co^{2+} ion [2] subject to a slight reduction in the periodic crystal. A reduction to 80 per cent of the free ion value gives the Coulomb Slater parameter $F^{(2)} = 7.54$ eV and $F^{(4)} = 5.11$ eV, but those parameters are not very critical for the low energy spectra. The free ion spectra are well fitted by a spin orbit coupling of $\zeta = 66$ meV (given for the one-electron basis) which coincides accidentally with the WF parameter.

The multiplet spectrum depends crucially on the ligand field part, which can be expressed in terms of Steven's operators. The cubic symmetry is broken due to the elongation of the octahedron along the c -axis and the ligand-field (or crystal-field) Hamiltonian is split into cubic and trigonal parts:

$$H_{\text{LF}} = H_{\text{cub}} + H_{\text{trig}} = -\frac{2}{3}B_4^0(O_4^0 - 20\sqrt{2}O_4^3) + B_2'O_2^0 + B_4'O_4^0 , \quad (5)$$

where the explicit expression of the Steven's operators is given in the book of Abragam and Bleaney [3], for example. There exist several notations for the three ligand field parameters for d -electrons in the trigonal case. Here we use the parameters Δ , v and v' like Koidl [4] and MacFarlane [5] (see also Ref. 6):

$$B_4^0 = -\frac{\Delta}{120} - \frac{1}{360} \left(v + \frac{3\sqrt{2}}{2}v' \right) , \quad B_4' = -\frac{1}{140} \left(v + \frac{3\sqrt{2}}{2}v' \right) , \quad B_2' = \frac{v - 2\sqrt{2}v'}{21} . \quad (6)$$

The LF and SO parameters are determined by a fit to the on-site Wannier expansion (2). Expressing (5) in terms of the trigonal basis (1) one finds the diagonal matrix elements

$$\langle x|H_0|x \rangle = \langle y|H_0|y \rangle = \frac{2}{5}\Delta + \frac{v}{3} , \quad \langle z|H_0|z \rangle = \frac{2}{5}\Delta - \frac{2}{3}v , \quad \langle v|H_0|v \rangle = \langle w|H_0|w \rangle = -\frac{3}{5}\Delta , \quad (7)$$

and the two off-diagonal elements (where we correct the misprinted sign of the v' term in [6])

$$\langle x|H_0|v \rangle = \langle y|H_0|w \rangle = -v' . \quad (8)$$

term	degeneracy	energy (eV)
${}^4T_{1g}$	12	0.00
${}^4T_{2g}$	12	0.77
2E_g	4	1.03
${}^4A_{2g}$	4	1.66
${}^2T_{1g}$	6	1.72
${}^2T_{2g}$	6	1.76
${}^4T_{1g}$	12	2.09

TABLE I. Predicted multiplet energies of Co^{2+} in $\text{Na}_2\text{BaCo}(\text{PO}_4)_2$. The Coulomb parameters $F^{(2)} = 7.54$ eV and $F^{(4)} = 5.11$ eV are chosen to have 80 per cent of their free ion value and the cubic crystal field splitting $\Delta = -0.8856$ eV of the Wannier fit is used. For the sake of clarity we neglect the spin-orbit coupling ζ and the small trigonal LF parameters v and v' .

v (meV)	v' (meV)	g_c	$g_{a/b}$	Δg	Δ_{Lines} (meV)
0	0	4.48	4.48	0.0	0.0
10	-10	4.33	4.55	-0.22	-2.1
10	0	4.81	4.31	0.50	9.6
4	4	4.80	4.31	0.49	8.5

TABLE II. g -factors for $\zeta = 66$ meV and varying trigonal distortion.

The other off-diagonal elements of (2) including the imaginary parts correspond to the SO coupling. So, we can simply read out the LF and SO parameters from the matrix (2) and find:

$$\begin{aligned}\Delta &= -885.9 \text{ meV}, & v &= 10.6 \text{ meV}, \\ v' &= -10.7 \text{ meV}, & \zeta &= 67.0 \text{ meV}.\end{aligned}$$

We remark a clear order of interactions as concerns the spin-orbit coupling and the ligand field parameter: $|\Delta| \gg \zeta \gg v, v'$. Also, the Wannier fit leads to practically the same spin-orbit coupling $\zeta = 67$ meV as that one obtained by fitting the optical spectra of a free Co^{2+} ion. That is surprising as we expect a reduction of the SO coupling in a crystal with respect to the free ion and can be explained by a slight overestimation of SO coupling in the GGA functional.

Taking into account the established order of interactions, we analyze first the multiplet spectrum neglecting the small trigonal distortion and the spin-orbit coupling (see Table I). The level scheme follows the general rules for a d^7 configuration in octahedral environment as treated in detail in the book of Abragam and Bleaney [3]. The lowest 4F multiplet of the free ion is split into ${}^4T_{1g}$, ${}^4T_{2g}$ and ${}^4A_{2g}$, where ${}^4T_{1g}$ is the lowest one for $\Delta < 0$ (octahedral environment). As can be seen in Tab. I, the ${}^4A_{2g}$ multiplet is higher than the lowest state with spin 1/2 (2E_g) in the given case.

Introducing the spin-orbit coupling of $\zeta = 66$ meV leads to a splitting of the ${}^4T_{1g}$ multiplet. In pure cubic symmetry the ${}^4T_{1g}$ multiplet can be described by an effective orbital moment $L_{\text{eff}} = 1$. Correspondingly, the spin-orbit splitting leads to an effective $\tilde{j}_1 = 1/2$ lowest doublet, followed by a $\tilde{j}_2 = 3/2$ quartet and a high-lying $\tilde{j}_3 = 5/2$ multiplet. In the ideal cubic case and neglecting any interaction to higher lying multiplets, the lowest doublet (effective spin 1/2) has an isotropic g -factor of $g = 4.33$. The trigonal distortion, i.e., the parameters v and v' , lead to anisotropic g -factors as presented in Table II. The WF parameter values $v = 10$ meV and $v' = -10$ meV lead to an opposite anisotropy $\Delta g = g_c - g_{ab} = -0.22$ with respect to the experimental results. But a slight correction recovers the correct order. That correction is not unique since v and v' influence the g -factor anisotropy in the form $\Delta g = (50v + 73v')/\text{eV}$ when all the other parameters are fixed and we present in Table II two parameter sets which lead to Δg being in reasonable agreement with experiment. We give in Table II also the trigonal splitting parameter Δ_{Lines} which was introduced by Lines [7] and used recently [8] to analyze $\text{Na}_3\text{Co}_2\text{SbO}_6$. It is defined as the trigonal splitting in the ${}^4T_{1g}$ multiplet when spin-orbit coupling is switched off.

The SO coupling parameter ζ for one d electron is related to $\lambda = -\zeta/3$ being the SO coupling between $S = 3/2$ and $L = 3$ in the 4F multiplet of a free ion. The effective SO coupling constant $\lambda = -3\lambda/2$ is defined as the coupling between $S = 3/2$ and $L_{\text{eff}} = 1$ in cubic symmetry. The theoretical SO coupling $\zeta = 66$ meV leads to the low-energy scheme which is shown in Table III with an energy difference $\Delta E_{\tilde{j}_1\tilde{j}_2} = 40.7$ meV (or 472 K) between the lowest $\tilde{j} = 1/2$ doublet and first excited quartet $\tilde{j} = 3/2$. As already noted in the main text, this theoretical energy difference lies in

	$\zeta = 66.0$ meV	$\zeta = 48.1$ meV
$\tilde{j} = 1/2$	0.0 meV	0.0 meV
$\tilde{j} = 3/2$	40.7 meV	30.0 meV
	45.6 meV	34.7 meV
$\tilde{j} = 5/2$	112.4 meV	84.0 meV
	113.6 meV	85.7 meV
	128.3 meV	93.7 meV
g_c	4.80	4.86
$g_{a/b}$	4.31	4.21

TABLE III. Comparison of energy splitting in the lowest multiplet ${}^4T_{1g}$ and of the g -factors for two different spin-orbit coupling parameters ζ . The trigonal LF parameters were chosen to be $v = v' = 4$ meV.

between the energy splittings deduced from the susceptibility data (419 K) and that one from the broadening of the ESR line width (510 K for the powder sample). The susceptibility data correspond to a SO coupling of $\zeta = 48.1$ meV (deduced from $\Delta E_{\tilde{j}_1 \tilde{j}_2} = 3\tilde{\lambda}/2 = 3\zeta/4$) and we show in Table III also the low-energy spectrum for this SO coupling parameter.

-
- [1] L. Giovanelli, A. Savoyant, M. Abel, F. Maccherozzi, Y. Ksari, M. Koudia, R. Hayn, F. Choueikani, E. Otero, P. Ohresser, J.-M. Themlin, S. Dhesi, and S. Clair, *J. Phys. Chem. C* **118**, 11738 (2014).
 - [2] www.nist.gov, [national institute of standards and technology, atomic spectra data base](http://www.nist.gov/pml/atomic-spectra-data-base) (2020).
 - [3] A. Abragam and B. Bleaney, *Electron paramagnetic resonance of transition ions*, Oxford classic texts in the physical sciences (Oxford University Press, 1970).
 - [4] P. Koidl, *Phys. Rev. B* **15**, 2493 (1977).
 - [5] R. M. MacFarlane, *J. Chem. Phys.* **47**, 2066 (1967).
 - [6] R. O. Kuzian, A. M. Daré, P. Sati, and R. Hayn, *Phys. Rev. B* **74**, 155201 (2006).
 - [7] M. E. Lines, *Phys. Rev.* **131**, 546 (1963).
 - [8] H. Liu, J. Chaloupka, and G. Khaliullin, *Phys. Rev. Lett.* **125**, 047201 (2020).
-